Desalination and Water Treatment
www.deswater.com
doi: 10.5004/dwt.2023.29915

308 (2023) 137–149
October

Improved photocatalytic performance under visible light of a novel Bi_2O_3-CdO-$CdCO_3$ ternary composite on glass wool

Kada Manseri[a], Imane Benyamina[a], Meriem Mansour[a], Mohamed Cherief[a], Salima Larbaoui[a], Abdelhadi Bentouami[a,*], Bruno Boury[b]

[a]*Laboratoire de Valorisation des Matériaux, Université de Mostaganem BP 227, Mostaganem 27000, Algeria, Tel.: +213 771 90 61 44; email: Abdelhadi.bentouami@univ-mosta.dz/Bentouami@gmail.com*
[b]*Institut Charles Gerhardt Montpellier, CNRS DR13, Route de Mende, 34095 Montpellier, France*

Received 14 May 2023; Accepted 23 August 2023

ABSTRACT

A novel ternary composite photocatalyst, Bi_2O_3-CdO-$CdCO_3$, was synthesized via a solvothermal method, followed by heat treatment at various temperatures with and without glass wool (GW). Characterization using X-ray diffraction (XRD), UV-Visible diffuse reflectance spectra, Brunauer–Emmett–Teller, scanning electron microscopy, and X-ray photoelectron spectroscopy confirmed the formation of nanomaterials. Photocatalytic activity was assessed by measuring the photo-discoloration of Indigo carmine dye under visible light and compared to CdO, Bi_2O_3, and TiO_2-P25. Remarkably, the highest efficiency was achieved with the GW-coated material treated at 400°C. XRD analysis revealed the presence of four phases in the non-calcined material, irrespective of GW presence. However, the 400°C treatment induced phase transformation, resulting in six phases in the material without GW and three phases in that with GW. Notably, GW presence influenced this transformation, yielding three dominant phases: Bi_2O_3, CdO, and $CdCO_3$, accounting for approximately 52%, 24%, and 24%, respectively, in contrast to the case without GW. The coexistence of these three phases on GW fibers significantly enhanced photocatalytic efficiency and longevity under visible light compared to the non-calcined material and material without GW.

Keywords: Photocatalyst; Ternary composite; Bi_2O_3-CdO-$CdCO_3$; Visible light; Indigo carmine

1. Introduction

Currently, metals oxides semiconductors have attracted wide scientific and technological research interest for their various applications such as photocatalysis [1], optoelectronics [2], photovoltaic [3,4] and more. Semiconductors are characterized by a valence band (VB) and a conduction band (CB). When the photonic energy is higher than band gap of semiconductor hence the latter absorbs this photonic energy, leading to the migration of an electron (e^-) from VB to CB, and the creation of a hole (h^+) on the VB [1]. As a result, strong active species, such as free radicals ($HO^\bullet$, $O_2^{\bullet-}$ and $HO_2^\bullet$), can be formed at the semiconductor surface from physisorbed molecules, such as H_2O and O_2. These free radicals and electron–hole pair can lead to redox reactions with pollutants at the solid-solution interface [5,6].

Related to their energy of their bandgap, some semiconductors are more photoactive under UV irradiation like (TiO_2, ZnO, ZnS, SnO_2 and $SrTiO_3$) than others more reactive under visible light as Bi_2O_3, Fe_2O_3, CdS, Bi_2WO_6. Besides, others are chemically unstable such as ZnO and CdS, even though they are widely applied as thin films in solar cells [7,8]. Moreover, as photocatalysts under visible light, CdS is more efficient than ZnS because the latter is very active only under UV. Nevertheless, CdS has low photocatalytic

* Corresponding author.

efficiency due to its low chemical stability in a slightly acidic solution with release of Cd^{2+} cations [9].

Cadmium oxide (CdO) is an *n*-type semiconductor with interesting properties, including a wide direct band gap of 2.27–2.86 eV [7–10] and a narrow indirect band gap of 0.55 eV [11,12]. Although CdO's applications in optoelectronic are well-documented, its use in photocatalysis has been less explored and is supported by a limited number of reports [13,14]. Nevertheless, doped CdO has been found to exhibit promising properties for antibacterial activity and herbicide degradation under UV irradiation, when combined with either Ag [15], or Zn [16]. CdO has also been successfully associated with other semiconductors in heterogeneous photocatalysis, such as ZnO for the discoloration of methylene blue under visible light [17], TiO_2 for the degradation of an azo dye (Reactive Orange) under UV-A irradiation [18], reduced graphene oxide (rGO) for methylene blue degradation under UV light [19], NiO for the degradation of Rhodamine B (RhB) under visible light [20], and ZnS for RhB degradation under UV-A irradiation [21].

Thanks to the narrow band gap energy of CdO (2.27–2.86 eV) [7–10,22] and Bi_2O_3 (2.3–2.84 eV) [23–25] compared to the medium band gap energy of $CdCO_3$ (3.79–3.87 eV) [7,26,27], as well as unlike the energy levels of the two conduction and valence bands of the three semiconductors (CdO, $CdCO_3$ and Bi_2O_3), it is possible that the ternary heterostructure material develops high photocatalytic efficiency under visible light due to good separation of the photo-generated electron–hole pair and minimization of their recombination.

This wide range in the energy of the band gap depends on the crystal structure of CdO, Bi_2O_3, and $CdCO_3$, which in turn, is influenced by the calcination temperature. For instance, Jeejamol et al. [22] found values of 2.57, 2.29, and 2.09 for CdO at calcination temperatures of 400°C, 600°C, and 800°C, respectively. These different values of E_g also modify the energies of the two conduction and valence bands.

The difference between the energy levels of the valence and conduction bands of each semiconductor can lead to efficient separation of the photo-generated electron–hole pair and minimize their recombination. To our knowledge, the synthesis of p-Bi_2O_3/n-CdO-$CdCO_3$ as heterostructure ternary composite has never been reported, so we have found it very interesting to target the preparation of this composite by the solvothermal synthesis route. Numerous composites based on Bi_2O_3 with other semiconductors have been reported, p-Bi_2O_3/n-ZnO [28–31], p-Bi_2O_3/n-TiO_2 [32–34]. To enhance the photocatalytic activity of doped semiconductors, various supports can be used to disperse the photocatalyst, increase the specific surface area and volume of pores, optimize light absorption, and enhance the interaction with pollutants. Supports like cotton [35], collagen [36], cellulose [37,38] and minerals like glass fiber [39–41], zeolites [42] graphene [43–45] and graphene oxide [46,47] can considerably improve photocatalytic efficiency compared to semiconductor alone. For the first time, in this work two novelties are presented, first synthesis of ternary composite Bi_2O_3-CdO-$CdCO_3$ (CBO) and secondly the glass wool (GW) working as an optically inactive material and as a support. The photocatalytic activity under low intensity of visible light (114.6 μW/cm²) of CBO was evaluated by photo-oxidation of Indigo carmine (IC) as dye model [5,28] and compared to benchmark materials (TiO_2-P25 and Bi_2O_3).

2. Experimental section

All starting chemicals of analytical purity, cadmium nitrate tetrahydrate ($Cd(NO_3)_2$ $4H_2O$); bismuth(III) nitrate pentahydrate ($Bi(NO_3)_3{\cdot}5H_2O$); urea (CH_4N_2O); glass wool (GW); ethanol (C_2H_5OH), diethylene glycol (DEG) ($(HOCH_2CH_2)_2O$); Indigo carmine (IC), or 5,5′-indigodisulfonic acid sodium salt ($C_{16}H_8N_2Na_2O_8S_2$) were obtained from Sigma-Aldrich Company and used without any purification.

2.1. Preparation of materials

All chemicals are of analytical grade and directly used as received. The preparation of our materials with or without glass wool fibers was carried out by the solvothermal method according to the following procedure with respect of Cd/Bi molar ratio of 10: solution A was made by dissolution $Cd(NO_3)_2$ $4H_2O$ (17.04 g, 0.055 mol) in DEG (10 mL), solution B: $Bi(NO_3)_3$ $5H_2O$ (2.68 g, 0.0055 mol) dissolved in DEG (10 mL), solution C: glass wool (GW) (100 to 500 mg) and urea (20.0 g, 0.333 mol) were dispersed in DEG (20 mL) using a 50 kHz Netzspannung ultrasound device. Solutions A, B and C were mixed and transferred into a Teflon-lined stainless-steel autoclave (100 mL) and placed in an oven at 150°C for 24 h. The obtained precipitate was separated by centrifugation (Hettich Rotofix 32) at 4,000 rpm for 10 min, washed thoroughly with deionized water (20 mL four times) and then with ethanol (10 mL once) and dried at 60°C for 24 h. The dried powder was then calcined in a muffle furnace at different temperature during 2 h. The obtained materials were named as CBO, CBO-GW, CBO-T and CBO-GW-T (according to cadmium; carbon; bismuth; oxygen, glass wool and T for calcination temperature).

2.2. Characterization of the prepared materials

Powder X-ray diffraction data were collected with monochromatic Cu $K\alpha_1$ radiation (λ = 1.54056 Å) at 40 kV and 30 mA using an Empyrean PANalytical diffractometer. The N_2 adsorption–desorption experiments at 77 K were carried out using a Micromeritics TriStar 3000. Samples were first treated to desorption at reduced pressure (<10^{-2}·Torr) at 150°C for 5 h. The specific surface area (SSA) was calculated using the Brunauer–Emmett–Teller (BET) method based on the adsorption isotherm and pore size distribution was calculated using the Barrett–Joyner–Halenda method on desorption isotherm branch. The morphologies of the prepared materials were observed by scanning electron microscopy (SEM) on Hitachi S-4800. The diffuse reflectance spectra (DRS) of the powder samples were recorded in the region of 200–1,000 nm on a UV-Visible spectrophotometer (Jasco V-670) equipped with an integrating sphere (Jasco PIN-757) using $BaSO_4$ as reference. X-ray photoelectron spectroscopy (XPS) data were obtained using an ESCALAB 250Xi Thermo electron spectrometer with monochromatic source of Al Kα (1,486.6 eV) radiation.

2.3. Study of heat treatment effect

Heat treatment at different temperatures has an effect on crystal and surface properties. These properties will have an effect on the photocatalytic properties of the obtained materials. The heat treatment was carried out in a muffle furnace at different temperatures (200°C, 300°C, 400°C, 500°C and 600°C) for 1 h. The photocatalytic efficiency was verified with 100 mg of each material in 100 mL of aqueous solution of IC at 44 mg/L. The magnetically stirred suspension was exposed to visible light. The result in the form of photo-discoloration yield was determined after separation by centrifugation and analysis of the supernatant by spectrophotometry at 610 nm using a JASCO V-730 UV-Visible spectrophotometer. The discoloration efficiency was determined by Eq. (1).

$$\text{yield}(\%) = \frac{\text{Abs}_t - \text{Abs}_0}{\text{Abs}_0} \times 100 \quad (1)$$

2.4. Photocatalytic activity evaluation

The photocatalytic activity of CBO-GW was evaluated in comparison with the commercial TiO_2-P25 Degussa, Bi_2O_3, CdO and CBO. In fact, under visible light irradiation, the photocatalytic discoloration experiments were conducted with 200 mL of Indigo carmine solution at different initial concentration, at natural pH 6.1 and with 1 g/L of solid/solution ratio using a 500 mL open Pyrex cylindrical beaker as photo-reactor. The latter was placed in a cooled bath with circulating water to keep the temperature stable at room temperature. The pH was measured at the beginning but not adjusted during the experiments. No oxygen was bubbled into the solution. Before lighting the lamp, the suspension was stirred in the dark during 30 min to establish the adsorption–desorption equilibrium. For each photocatalyst, the evaluation was achieved when the discoloration was done. The visible light lamp was positioned 17 cm above the beaker. The characteristics of the lamp used in this study are mentioned in our previous work [5,23,28].

2.5. Identification of active species

In order to determine which species are active in the photo-discoloration of Indigo carmine under visible light, four radical scavengers were used: ascorbic acid (2 mmol/L) to trap the superoxide anion radical, ethanol (2 mmol/L) to scavenge the $HO^{\bullet}$ radical, disodium ethylenediaminetetraacetate (Na_2EDTA, 1 mmol/L) to inhibit holes (h^+) activity, and $AgNO_3$ (1 mmol/L) to trap electrons (e^-) [5,23,28,48,49]. The experiments were conducted using 100 mg CBO-GW-400 and 100 mL dye solution at a concentration of 44 mg/L and at a natural pH of 6.1. After sampling and centrifuging the aliquots, the dye concentration in the supernatants was determined.

2.6. Reusability study

The stability and longevity of the best photocatalyst namely CBO-GW-400 was evaluated for an initial concentration of Indigo carmine of 44 mg/L at natural pH 6.1 with a photocatalyst concentration of 1 g/L. After contacting under magnetic stirring in the dark for 30 min, the suspension was then exposed to visible light until complete discoloration after 30 min. Then the photocatalyst was separated from the mixture by centrifugation and dried at 100°C for 3 h, unground then added to a new IC solution at the same concentration as the first and under the same conditions. The stability of the photocatalyst was thus verified in the photocatalytic discoloration of the IC five times.

3. Results and discussions

3.1. Heat treatment temperature effect

In order to determine the optimum temperature for heat treatment, calcination of CBO was carried out at different temperatures and the resulting calcined photocatalysts were tested. Fig. 1 presents the results in a histogram form, showing the effect of heat treatment on the photocatalytic discoloration efficiency of IC at an initial concentration of 44 mg/L. The material treated at 400°C (CBO-GW-400) showed the highest efficiency, achieving complete discoloration after just 30 min of visible light irradiation. In contrast, CBO-GW (uncalcined), CBO-GW-200, CBO-GW-300, CBO-GW-500, and CBO-GW-600 achieved only 45.83%, 72.56%, 83.67%, 97.09%, and 80.56% discoloration, respectively. There may be several explanations for this difference in efficiency: heat treatment above 400°C probably modified the crystalline phases by, perhaps initiating the transformation of $CdCO_3$ to CdO, altering surface properties such as specific surface area and pore diameter, and probably the alteration of optical properties such as band-gap energy. Consequently, only materials prepared with and without GW and treated at 400°C were characterized. In addition, the study of photo-discoloration of IC was continued with CBO-GW-400 and CBO-400.

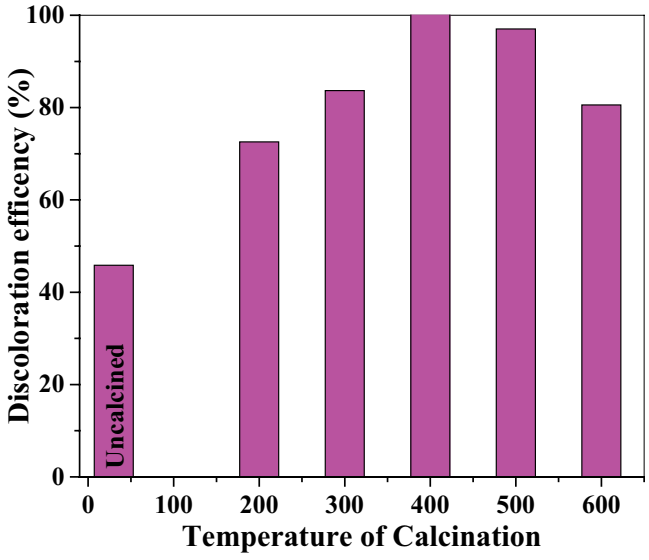

Fig. 1. Heat treatment effect on photocatalytic efficiency.

3.2. Characterizations of materials

3.2.1. Powder X-ray diffraction analysis

In diffractograms (Fig. 2A and B) of materials before calcination without and with GW, respectively, the indexed peaks are characteristic of a mixture of four composites: bismutite $Bi_2(CO_3)_2O_3$ (JCPDS 25-1464), otavite $CdCO_3$ (JCPDS 42-1342), bismuth trihydroxide $Bi(OH)_3$ (JCPDS 01-0898) and the rhombohedral phase of bismuth metal Bi (JCPDS 44-1246), with a slight dominance of two composites – bismutite and otavite – according to the intensity of their diffraction peaks plans (103) for bismutite and (012) for otavite. The thermal treatment at 400°C led to significant crystallographic changes, particularly the formation of oxides and the disappearance of bismutite, Bi and bismuth trihydroxide, (Fig. 2C and D). However, in the absence of GW, characteristic peaks of four phase is observed: CdO (JCPDS 75-0594), $CdCO_3$ (JCPDS 42-1342), $Bi_{7.79}Cd_{0.21}O_{11.9}$ (JCPDS 49-1763), monoclinic α-Bi_2O_3 (JCPDS 29-0236) and tetragonal β-Bi_2O_3 (JCPDS 41-1449). Differently, for the material prepared with GW, the diffractograms show characteristic peaks of only three composites, namely CdO, $CdCO_3$ and β-Bi_2O_3, with a predominance of the latter, as indicated by the peak of *hkl* plane (201). Additionally, the characteristic peaks of $CdCO_3$ appear with slightly higher intensities than those of CdO. Therefore, the presence of GW and heat treatment at 400°C lead to the formation of a ternary composite comprising β-Bi_2O_3, $CdCO_3$, and CdO. In a study by Lim et al. [50], an α/β phase heterojunction of Bi_2O_3 electrospun nanofibers was synthesized, and they found that only the β phase was obtained at room temperature up to 325°C, with the transformation of the β phase to α achieved by thermal treatment from 350°C. Here, the β phase remains stable up to 400°C when GW was used in the solvothermal synthesis.

The estimated compositions based on the most intense peak of each phase is 52% β-Bi_2O_3, 24% CdO, and 24% $CdCO_3$ for CBO-GW-400. In contrast, CBO-400 exhibited six phases with a composition of 22.7% β-Bi_2O_3, 30.44% $CdCO_3$, 23.34% CdO, 10.50% $Bi_{7.79}Cd_{0.21}O_{11.90}$, 7.24% α-$Bi_2O_3$, and 5.78% Bi_2O_4.

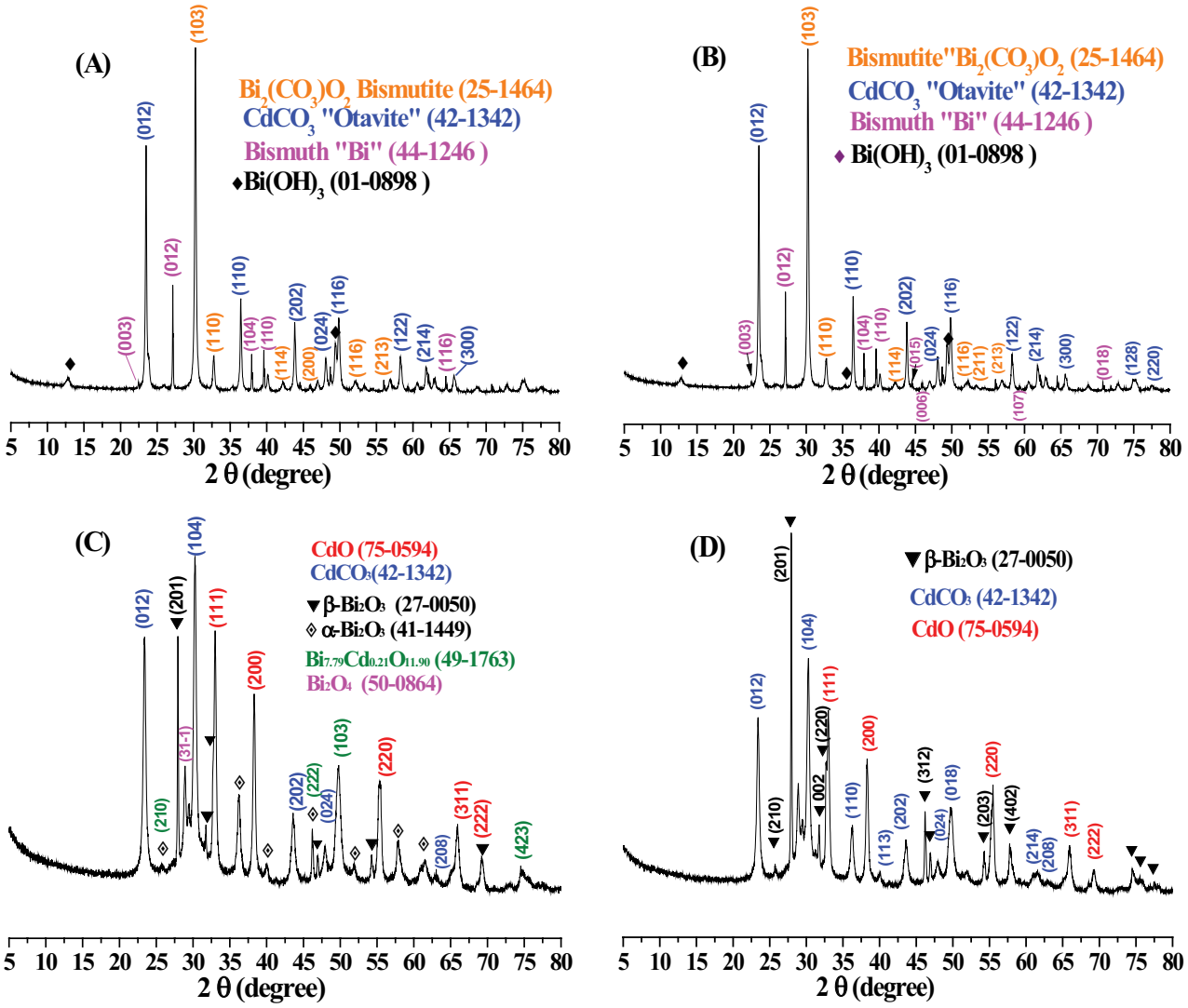

Fig. 2. XRD patterns of CBO (A), CBO-GW (B), CBO-400 (C) and CBO-GW-400 (D).

It is evident that the material prepared with GW has a significantly higher proportion of β-Bi_2O_3 compared to the other phases. This observation may favor its photocatalytic activity under visible light, as β-Bi_2O_3 has a narrower band gap energy compared to other present phases.

The crystallite size (*D*) was calculated from the most intense pick of each phase using Scherrer's formula presented in Eq. (2):

$$D = \frac{0.9\lambda}{\beta\cos\theta} \quad (2)$$

where λ is the wavelength of X-ray radiations (λ = 1.5408 Å), 0.9 is the Scherrer's constant, θ is the Bragg angle between the incident ray and the diffracted plane, and β is the full width at half maximum (FWHM) of the peaks. It seems that there is no general trend that can be deduced from reported crystallite size values in Table 1 concerning any effect of GW.

Table 1
Phase composition and crystallite size

Phase type	CBO-400		CBO-GW-400	
	%	*D* (nm)	%	*D* (nm)
β-Bi_2O_3	22.7	58.05	52	87.84
CdO	23.34	59.17	24	31.80
$CdCO_3$	30.44	37.94	24	36.96
α-Bi_2O_3	7.24		0	
$Bi_{7.79}Cd_{0.21}O_{11.90}$	10.5		0	
Bi_2O_4	5.78		0	

3.2.2. BET specific surface area analysis

Fig. 3A and B show the N_2 adsorption–desorption isotherms at 77 K for CBO-400 and CBO-GW-400, respectively. Both isotherms exhibit type IV forms with H_3 type hysteresis loops, indicating a mesoporous structure for both photocatalysts. The BET surface area, pore size, and total pore volume of both materials are summarized in Table 2.

The presence of GW in the synthesis of CBO-GW-400 has no impact on the BET surface area that is similar in both cases SSA ~ 10 m^2/g. The external surface area of CBO-GW-400 was more than double that of CBO-400, indicating a higher degree of surface roughness in CBO-GW-400. The addition of GW also led to an average pore size that was 20% smaller, which should be taken into consideration when analysing the photocatalytic performance. Similar observations were reported by Benyamina et al. [28] and Mansour et al. [23].

3.2.3. SEM analysis

Comparison of the morphology and shape of GW before photocatalyst (Fig. 4A) synthesis, CBO-GW-400 (Fig. 4B) and CBO-400 (Fig. 4C and D) observed by SEM, shows that CBO-GW-400 has irregular flake-like structures of photocatalyst attached to the surface of the GW fiber (Fig. 4B). Different shapes specific to the three compounds are also observed next to the fiberglass. For CBO-400, different particles shapes are tentatively attributed to sand-roses-of Bi_2O_3, irregular cube for CdO and cauliflower-like particles $CdCO_3$ (Fig. 4C and D), Similar observations have been reported by Jia et al. [51] for CdO prepared using a solvothermal process with an ethylene glycol/H_2O solution.

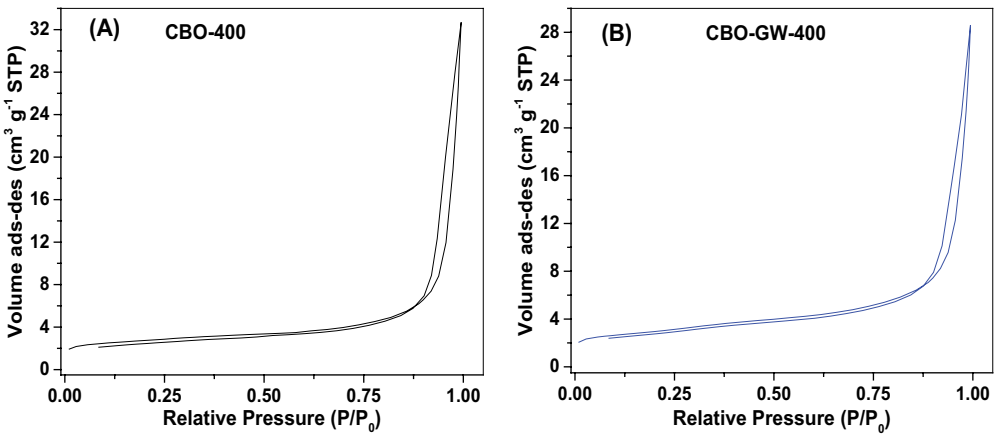

Fig. 3. N_2 adsorption–desorption isotherms of (A) CBO-400 and (B) CBO-GW-400.

Table 2
Textural properties of prepared composites obtained from adsorption–desorption of N_2 at 77 K

Samples	A_{BET} (m^2/g)	A_{Ext} (m^2/g)	V_t (cm^3/g)	M_{meso} (cm^3/g)	$V\mu$ (cm^3/g)	Pores size (nm)
CBO-400	9.41	4.33	0.051	0.048	0.002	34.88
CBO-GW-400	10.25	9.1	0.044	0.044	0.0006	28.31

3.2.4. UV-Vis DRS analysis

Analysis by UV-Vis diffuse reflectance spectroscopy (Fig. 5) was used to determine the band gap energy and the electronic transition type (according to the Kubelka–Munk (K-M)) model as a function of reflectance (R) Eq. (3) proposes two constants α (absorption coefficient) and s the diffusion coefficient [52–54],

$$F(R)=\frac{(1-R)^2}{2R}=\frac{K}{S}\approx\frac{\alpha}{s} \tag{3}$$

where K and S are the K-M absorption and scattering coefficients, respectively and, α is related to the wavelength and the energy of the band gap (E_g), according to Tauc's equation [Eq. (4)]. where h, ν, and β are the Planck's constant (J/s), the light frequency (s^{-1}) and the proportionality coefficient, respectively.

$$(\alpha h\upsilon)=\beta(h\upsilon-E_g)^n \tag{4}$$

The n value depends on the electronic transition type between the valence and conduction bands and can be 1/2 or 2 for a direct or indirect transition, respectively.

Eq. (5) can be modified as Eq. (6), where α can be replaced by $F(R)$.

$$(F(R)h\upsilon)=\beta(h\upsilon-E_g)^n \tag{5}$$

And

$$\ln[F(R)h\upsilon]=\ln\beta+n\ln[(h\upsilon-E_g')] \tag{6}$$

The determination of the electronic transition type according to several authors [55] can be carried out in two steps which can be followed in order to determine the value of n. First, the K-M function ($F(R)$) will be plotted vs. $h\upsilon$ energy and then the extrapolation of linear part of the plot to x-axis gives the assumed value of band gap energy (E_g'). Second, plotting logarithm of modified Tauc's equation vs. logarithm of $h\upsilon$ Eq. (6) allows us to determine the mathematical equation of linear part of the plot. The slope of the equation represents the value of n. Thus, plots of the first step are shown in Fig. 5A for CBO-GW-400 and in Fig. 5B for CBO-400. Then those of the second step are in Fig. 5C and D, respectively.

The values of the slopes ~0.65 indicates an indirect electronic transition, that is, n = 0.5. Based on these results, the energy values of band gap of the prepared materials were determined by plotting $(F(R)\cdot h\upsilon)^2$ vs. $h\upsilon$ (Fig. 5E and F) and are 2.25 and 2.27 eV for CBO-GW-400 and CBO-400, respectively. The effect of GW during the synthesis leads to a slightly reduced band gap for material prepared

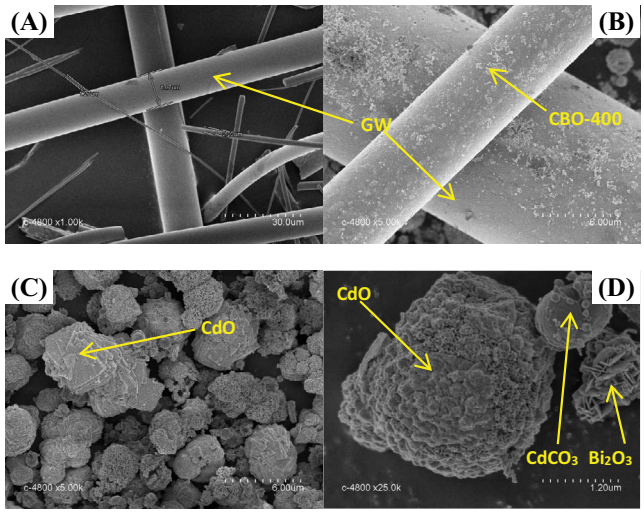

Fig. 4. SEM images of (A) virgin GW, (B) CBO-GW-400, (C) and (D) CBO-400.

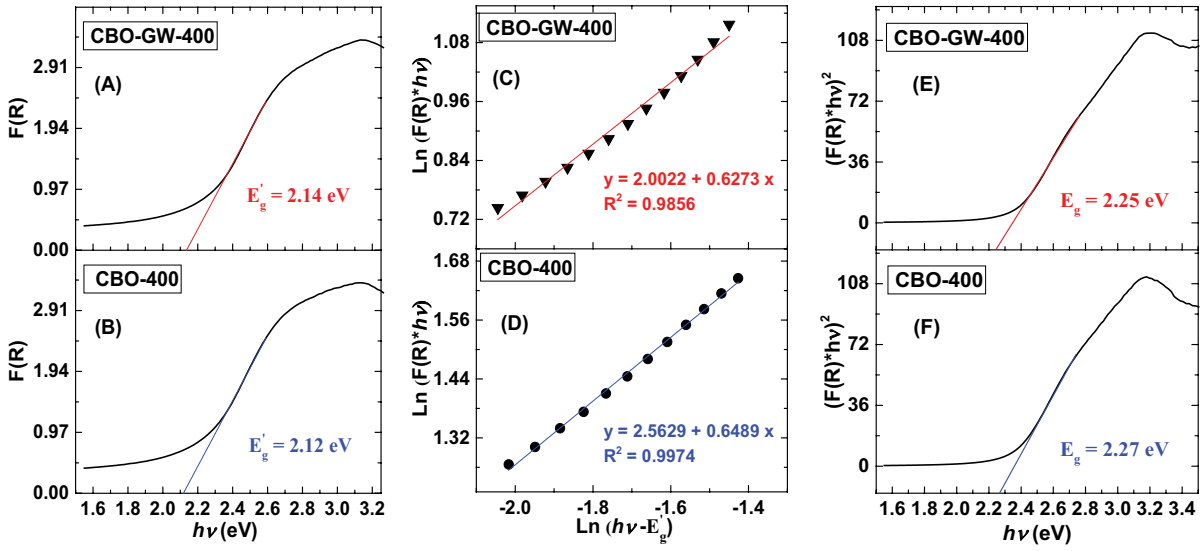

Fig. 5. Kubelka–Munk plot vs. $h\upsilon$ (A and B), logarithm modified Tauc function plot vs. ln($h\upsilon$) (C and D) and plot of indirect electronic transition (E and F) for prepared photocatalysts.

without GW which may be beneficial for photocatalysis under visible light.

3.2.5. XPS analysis

The chemical state of atoms and their composition on the surface of the prepared materials was carried out by XPS. After deconvolution, the XPS spectra of Bi 4f, Cd 3d, C 1s and O 1s of the two calcined materials are presented in Fig. 6. For the values of the binding energies of Bi $4f_{5/2}$ are 163.89 and 164.36 eV and those of Bi $4f_{7/2}$ are 158.58 and 159.04, respectively CBO-400 (Fig. 6A) and CBO-GW-400 (Fig. 6B). The Bi 4f (E Bi 4f) core level increases from 0.5 eV towards higher binding energy for CBO-GW-400 compared to CBO-400. The positive shifts to higher binding energies probably indicate that the bismuth oxide species for the CBO-GW-400 material are strongly bound to the GW surface or else strong interactions are present between CdO and $CdCO_3$ when GW was used. The Cd 3d spectral line revealed two intense peaks at 412.1 and 405.3 eV for CBO-400 (Fig. 6C) and at 412.5 and 405.8 eV for CBO-GW-400 (Fig. 6D) attributed to $3d_{3/2}$ orbitals and $3d_{5/2}$, respectively. Same observation made for Cd than Bi, the Cd 3d core level increases by 0.3–0.5 eV towards higher binding energy for CBO-GW-400 compared to CBO-400. This shift to high binding energies likely indicates that the cadmium oxide and cadmium carbonate species for the CBO-GW-400 material are strongly bonded to each other and between Bi_2O_3

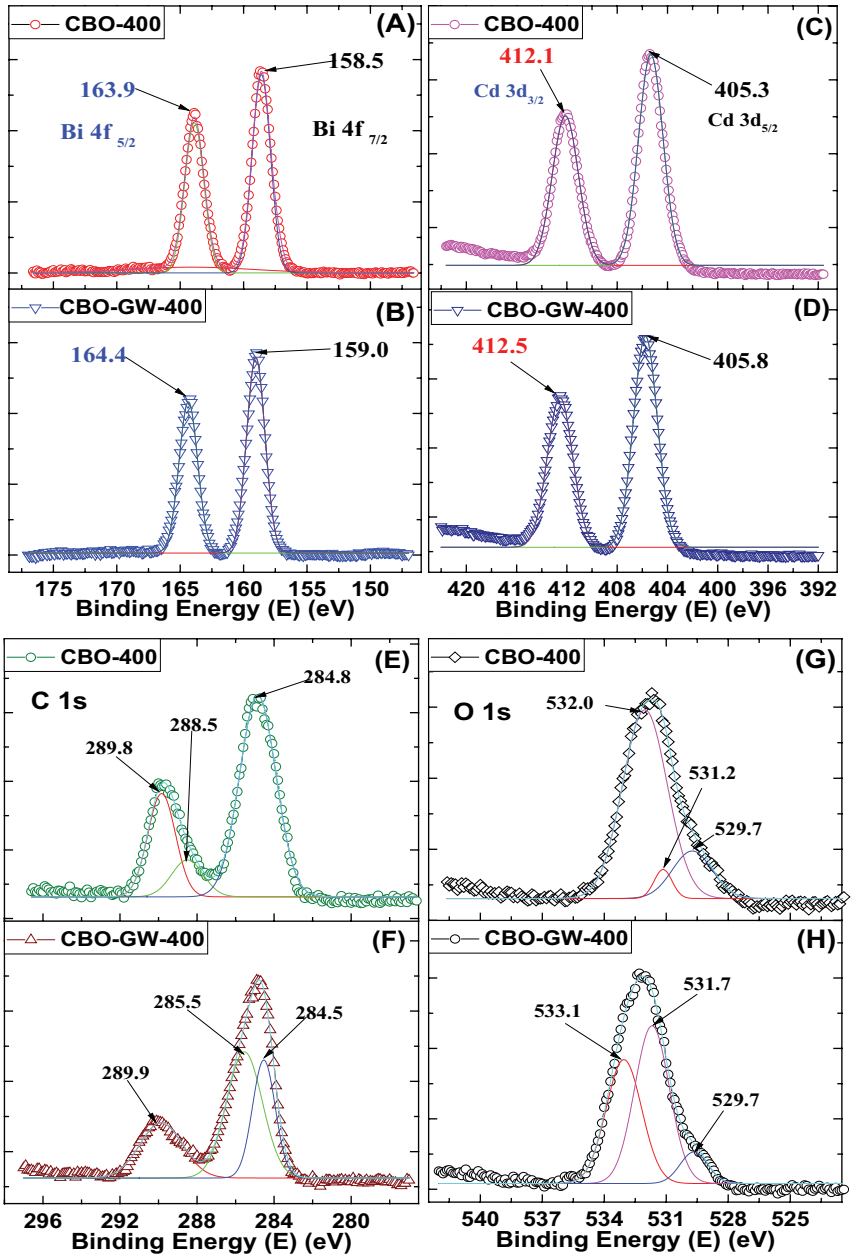

Fig. 6. Deconvoluted XPS spectra of Bi 4f (A and B), Cd 3d (C and D), C 1s (E and F) and O 1s (G and H).

and possibly are tightly bonded to the GW surface compared to the material without the GW (CBO-400). The C 1s level (Fig. 6E and F) shows the presence of three different carbon environments in the two photocatalysts with also varied intensities between the materials. First, the binding energy at 284.8 eV for CBO-400 and at 284.5 eV for CBO-GW-400 is attributed to C–C [56–59] of the adventitious carbon. Moreover, the C 1s intensity at 284.8 eV is higher for the CBO-400 material than that at 284.5 eV for CBO-GW-400. This leads us to suppose that first the organic carbon impurities are lower in CBO-GW-400 than in CBO-400 and secondly are somewhat different 288.5 eV to C=O and 285.5 eV correspond to C–O. Besides, the binding energy at 289.8 eV in CBO-400 and 289.9 eV in CBO-GW-400 correspond to O–C=O [43–47]. However, the peak intensity at 289.8 eV is higher in CBO-400 than that at 289.9 eV in CBO-GW-400, a difference attributed to higher $CdCO_3$ content in CBO-400 than in CBO-GW-400 in agreement with X-ray diffraction (XRD) results (Table 1). The deconvoluted O 1s spectrum (Fig. 6G and H) shows three distinct peaks at 529.7, 531.2 and 532.0 eV in CBO-400 and at 529.7, 531.7 and 533.1 eV in CBO-GW-400 are assigned, respectively to the Bi–O, Cd–O and O–C bonds [5,23,28,31,51].

3.3. Photocatalytic activity study

3.3.1. Comparative study

A comparative study was conducted to determine the photocatalytic efficiency of CBO-GW-400 and CBO-400, as well as reference materials CdO, Bi_2O_3, and TiO_2-P25. The efficiency was determined by the discoloration of an aqueous solution of IC with a concentration of 44 mg/L under visible light at room temperature. IC was chosen as an appropriate model dye in comparison to the results obtained in our previous work [5,28]. The results presented in Fig. 7 demonstrate that both CBO-GW-400 and CBO-400 exhibited higher photocatalytic efficiency than the other tested photocatalyst.

It is clear from the histogram of Fig. 7 that GW exhibits the low removal rate probably due to adsorption, because GW is an optically inactive silica oxide-based material. Moreover, TiO_2 is known to be highly effective only under UV irradiation, which is why the discoloration rate obtained with TiO_2 is low compared to other photocatalysts under visible light. On the other hand, despite that Bi_2O_3 and CdO are photocatalysts with narrow bandgap energies, they also exhibit low photo-discoloration rates under visible light, which could be explained by the rate of e^-/h^+ recombination that can be high according to the literature [60–64].

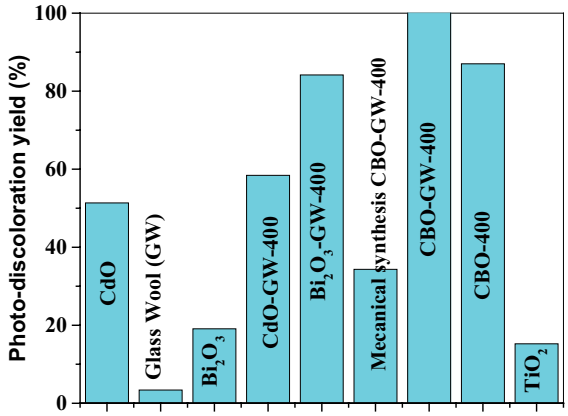

Fig. 7. Comparative study between prepared and benchmark materials on photocatalytic discoloration under visible light after 30 min of IC at 44 mg/L.

3.3.2. Kinetics of photo-discoloration

Kinetic of discoloration is shown in Fig. 8A and B for CBO-GW-400 and CBO-400, respectively, by plotting the C_t/C_i ratio vs. contact time. A slightly higher dye adsorption prior to photodegradation is observed for CBO-400 compared to CBO-GW-400. However, the photodegradation kinetics, are faster with CBO-GW-400 than with CBO-400, with 97.42% discoloration achieved after 20 min for CBO-GW-400 and only 81.75% for CBO-400. Furthermore, total discoloration is achieved after 30 min in the presence of CBO-GW-400, compared to only 87.09% achieved in the presence of CBO-400.

3.3.3. Kinetics modelling

The parameters of the photocatalytic discoloration kinetics were determined by applying the pseudo-first-order kinetic model, as described by Eq. (7):

$$\ln\left(\frac{C_{i,\mathrm{corr}}}{C_t}\right) = k_{\mathrm{app}} t \tag{7}$$

where C_t and $C_{i,\mathrm{corr}}$ (mg/L) are respectively the dye concentration at time t and the corrected initial dye concentration (after adsorption in the dark). The k_{app} (min^{-1}) represents the kinetics constant. From plots of $\ln(C_{i,\mathrm{corr}}/C_t)$ vs. time t (Fig. 8C and D) for respectively CBO-GW-400 and CBO-400, the kinetic constant for each dye concentration was determined. These values are also plotted in histogram form (Fig. 8E). The kinetic constant of CBO-GW-400 is approximately 1.4 to 2 times higher than those obtained with CBO-400.

The CBO-GW-400 material exhibits higher photocatalytic efficiency than CBO-400. This difference is likely attributed to several factors, even though both materials have almost identical bandgap energy of about 2.2 eV. Notably, CBO-GW-400 possesses an external surface area twice as large as CBO-400. Furthermore, XRD results indicate that CBO-400 consists of six phases, while CBO-GW-400 contains only three phases. This compositional difference in phases between CBO-400 and CBO-GW-400 may account for the lower efficiency observed in CBO-400. In CBO-GW-400, both CdO and $CdCO_3$ are present at 24%, whereas in CBO-400, the $CdCO_3$ level is higher (30.44%) than that in CBO-GW-400. Additionally, the rate of the β-Bi_2O_3 phase is more than double compared to CBO-400.

3.3.4. Identification of active species

Four main radical species can be at the origin of the photocatalytic efficiency of the material acting individually

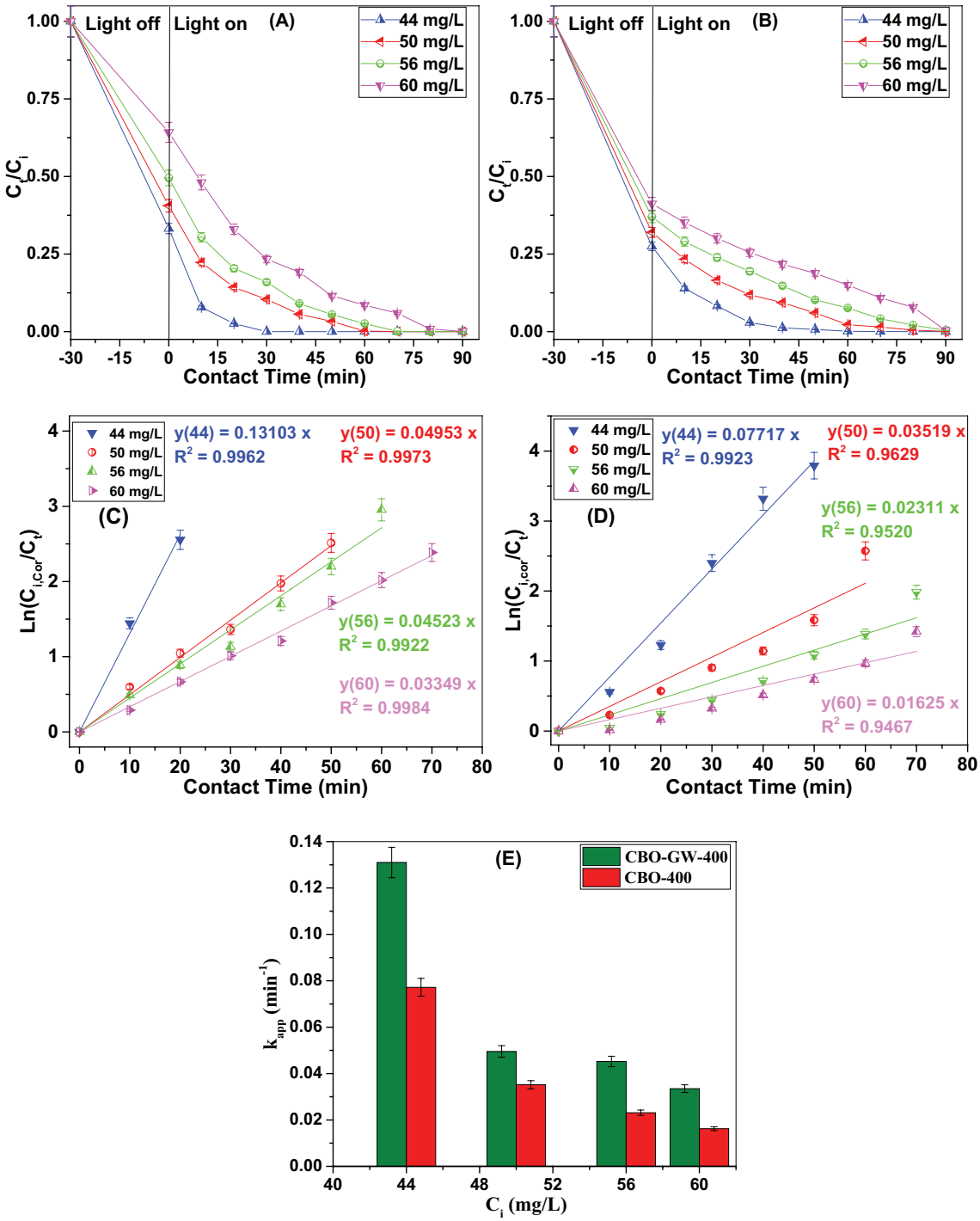

Fig. 8. (A and B) Kinetics of photo-discoloration under visible light at different concentrations of IC by CBO-GW-400 and CBO-400 respectively, (C and D) modeling the kinetics of photo-discoloration for CBO-GW-400 and CBO-400 respectively, and (E) evolution of K_{app} as a function of IC initial concentration.

or mutually. These radicals can be identified by adding the scavengers for each species, the superoxide radical, the hydroxyl radical, the photo-generated holes and electrons each.

The C_t/C_i plots vs. contact time in Fig. 9 exhibit the effect of each scavenger on the yield of photocatalytic efficiency of CBO-GW-400. It should be noted that complete discoloration was observed after 30 min when no scavengers were added. Furthermore, the same result was obtained in the presence of ascorbic acid (a scavenger of the superoxide anion radical). This radical is formed by the reaction between oxygen (O_2) and the electron (e^-) in the conduction bands. The fact that the presence of ascorbic acid had no effect on the yield indicates that the superoxide anion radical is

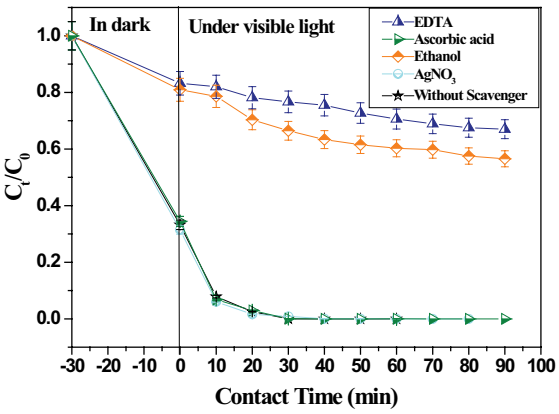

Fig. 9. Identification of the radical species responsible for the IC dye photo-discoloration under visible light by CBO-GW-400.

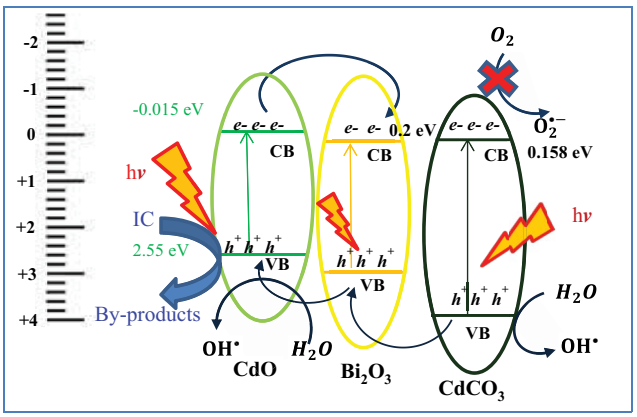

Fig. 10. Diagram illustrating the diagram of the energy levels of the conduction and valence bands of the three semiconductors making up the CBO-GW-400.

absent in the photo-discoloration mechanism. This absence can be explained by the non-reaction between oxygen and electrons from the conduction bands of the three semiconductors present in the CBO-GW-400 material. Indeed, when the $AgNO_3$ (electron scavengers) was added, the photocatalytic efficiency did not drop compared to the case without scavengers. However, the photo-discoloration efficiency drops to 33.56% in the presence of ethanol (a scavenger of hydroxyl radicals, $HO^{\bullet}$) and down to 23.35% when EDTA (a hole scavenger) is added. The results obtained from this study indicate that the h^+ species contributes significantly to the photo-discoloration of the IC dye, while the hydroxyl radical plays a moderate role. The contribution of the superoxide anion radical is found to be absent. Therefore, photo-discoloration in the presence of CBO-GW-400 occurs in a mutual manner between holes and hydroxyl radicals.

3.3.5. Suggested photocatalytic mechanism

Looking at the CBO-GW-400 photocatalyst as a material containing three semiconductors; namely Bi_2O_3, CdO, and $CdCO_3$; as indicated by the XRD results. These three semiconductors have band gap energies with values of 2.84, 2.57, and 3.79 eV, respectively, according to the literature [7,22,23]. Consequently, their energy levels at the conduction and valence bands can be calculated using Eqs. (8) and (9):

$$E_{VB} = \chi - E_C + 0.5E_g \quad (8)$$

$$E_{CB} = E_g - E_{VB} \quad (9)$$

where E_C is the energy of free electrons on the scale of hydrogen, around 4.5 eV. And χ is the absolute electronegativity of the samples represents the absolute electronegativity of each photocatalyst determined by the geometric mean of the electronegativity of each atom calculated according to Mulliken scale. Thus, the value of χ of CdO, $CdCO_3$ and Bi_2O_3, are respectively 5.77, 6.55 and 6.12 eV. According Eqs. (8) and (9); the value of E_{VB} and E_{CB} are respectively 2.555; –0.015 eV for CdO; 3.94, 0.158 eV for $CdCO_3$ and 3.04, 0.2 eV for Bi_2O_3 (vs. NHE). A diagram illustrating the energy levels of the conduction and valence bands of the three semiconductors constituting the photocatalyst can be proposed in Fig. 10.

The fact that the bandgap energy (E_g = 3.78 eV) of $CdCO_3$ is greater than the photonic energy coming from the visible lamp (λ > 400 nm or E < 3.2 eV), this implies that the electrons of the valence bands (VB) of Bi_2O_3 and CdO only, will be excited and migrate to the conduction bands (CB). This process creates the electron/hole (e^-/h^+) pairs (R1).

It is assumed that the oxidation reactions of the IC dye would occur through the h^+ in the VB of $CdCO_3$, Bi_2O_3 and CdO, as they possess high energy levels (R2).

Moreover, H_2O molecules would react with the holes in the VB of all three semiconductors, as the potential of the $HO^{\bullet}/H_2O$ pair with a value of 1.99 eV (vs. NHE) is much lower than that of the VBs of all three semiconductors (R3). As a result, the hydroxyl radical ($HO^{\bullet}$) will oxidize the IC dye (R4). However, dissolved oxygen should not act as an oxidant by accepting electrons from the CBs to form the superoxide anion radical ($O_2^{\bullet-}$), as the potential of the $O_2^{\bullet-}/O_2$ couple (–0.044 eV vs. NHE) is lower than the energy levels of the CBs of the three semiconductors comprising the CBO-GW-400 material. This could explain the absence of the $O_2^{\bullet-}$ radical species in the IC dye degradation process, as supported by the results of the scavenger's study effect on the degradation efficiency. Electron–hole (e^-/h^+) recombination seems absent or negligible (R5). Thus, the mechanism of photo-discoloration of IC dye by CBO-GW-400 could be suggested as a combination of the following reactions:

$$\text{CBO} - \text{GW} - 400 + h\nu \rightarrow \text{CBO} - \text{GW} - 400\left(e^-, h^+\right) \quad (R1)$$

$$h^+ + \text{Indigo Carmine} \rightarrow \text{by-products}\ \left(\text{Major reaction}\right) \quad (R2)$$

$$h^+ + H_2O \rightarrow HO^{\bullet} + H^+ \quad (R3)$$

$$HO^{\bullet} + \text{Indigo Carmine} \rightarrow \text{by-products}\ \left(\text{Moderate reaction}\right) \quad (R4)$$

$$h^+ + e^- \rightarrow \left(e^-, h^+\right)\ \left(\text{Negligible recombination reaction}\right) \quad (R5)$$

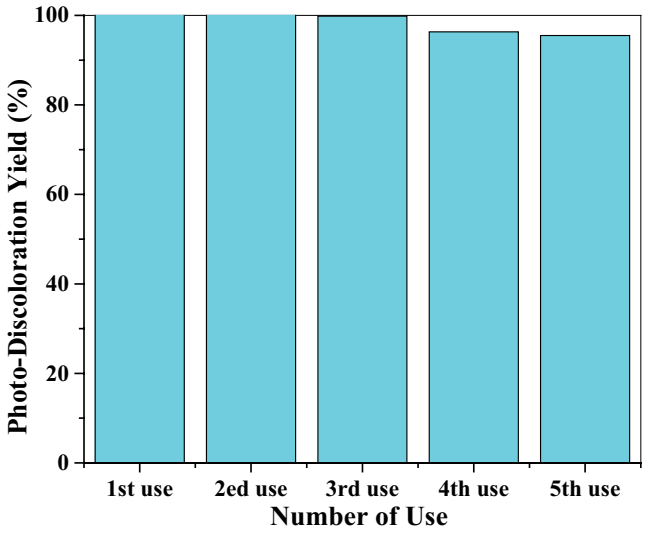

Fig. 11. Stability and longevity study of CBO-GW-400.

3.3.6. Stability and longevity study

The stability of the CBO-GW-400 was assessed after five uses (Fig. 11), revealing a slight decrease in effectiveness after the fourth use. Specifically, a reduction of approximately 3.68% was observed after four uses, with a further 4.5% decrease after five uses. However, these changes are within acceptable limits for photocatalysts, in CBO-GW-400 is stable photocatalyst that retains its effectiveness even after five uses. This can be attributed to the good separation e^-/h^+ pairs and a low recombination rate.

4. Conclusion

This study demonstrates the solvothermal preparation of the heterostructure CdO-Bi_2O_3-$CdCO_3$ ternary in DEG/water medium. An optimal thermal treatment at 400°C has been determined, higher or lower temperature leading to less efficient materials. The high efficiency of visible light photodegradation is attributed to the combination of three components: 52% β-Bi_2O_3, 23.8% CdO and 24% $CdCO_3$. Additionally, using glass wool as a cheap, non-toxic support has the potential to slightly improve efficiency. Indeed, this improved efficiency with longevity of five uses obtained with the photocatalyst prepared with GW is probably due to the presence of the β-Bi_2O_3 phase at 52% in CBO-GW-400, against 22.7% in the sample prepared without GW. Additionally, the lower level of $CdCO_3$, 24% in CBO-GW-400 compared to 30.44% in CBO-400, could also contribute to this improvement. Thus, the presence of twice as much β-Bi_2O_3 phase in CBO-GW-400 than in CBO-400 could provide an advantage in terms of efficiency. Moreover, the use of GW allows an increase in surface properties and the formation of three compounds, which led to photocatalytic enhancement compared to the material prepared without GW (which contained five compounds). IC photo-discoloration in the presence of CBO-GW-400 occurs in a mutual manner between holes and hydroxyl radicals. Accordingly, under visible light irradiation, holes and hydroxyl radicals played a key role in the degradation of IC. The absence of the role of the superoxide anion radical ($O_2^{\bullet-}$) in the degradation mechanism of IC dye has been demonstrated through scavenger studies and supported by the diagram showing the higher energy levels of the conduction bands of the three semiconductors composing the photocatalyst by relative to the potential of the $O_2^{\bullet-}/O_2$ couple. Accordingly, under visible light irradiation, holes and hydroxyl radicals played a key role in the degradation of IC by CBO-GW-400.

Acknowledgements

This work is part of a project (A16N01UN270120200005) funded by the thematic science and technology research agency (ATRSDT) of the general direction of scientific research and technological development (DGRSDT) within the Algerian ministry of higher education and scientific research.

References

[1] H. Wang, L. Zhang, Z. Chen, J. Hu, S. Li, Z. Wang, J. Liu, X. Wang, Semiconductor heterojunction photocatalysts: design, construction, and photocatalytic performances, Chem. Soc. Rev., 43 (2014) 5234–5244.
[2] D.V. Talapin, J.-S. Lee, M.V. Kovalenko, E.V. Shevchenko, Prospects of colloidal nanocrystals for electronic and optoelectronic applications, Chem. Rev., 110 (2010) 389–458.
[3] A.J. Nozik, M.C. Beard, J.M. Luther, M. Law, R.J. Ellingson, J.C. Johnson, Semiconductor quantum dots and quantum dot arrays and applications of multiple exciton generation to third-generation photovoltaic solar cells, Chem. Rev., 110 (2010) 6873–6890.
[4] H.-Q. Wang, M. Batentschuk, A. Osvet, L. Pinna, C.J. Brabec, Rare-earth ion doped up-conversion materials for photovoltaic applications, Adv. Mater., 23 (2011) 2675–2680.
[5] B. Benalioua, M. Mansour, A. Bentouami, B. Boury, E.H. Elandaloussi, The layered double hydroxide route to Bi–Zn co-doped TiO_2 with high photocatalytic activity under visible light, J. Hazard. Mater., 288 (2015) 158–167.
[6] M. Pelaez, N.T. Nolan, S.C. Pillai, M.K. Seery, P. Falaras, A.G. Kontos, P.S.M. Dunlop, J.W.J. Hamilton, J.A. Byrne, K. O'Shea, M.H. Entezari, D.D. Dionysiou, A review on the visible light active titanium dioxide photocatalysts for environmental applications, Appl. Catal., B, 125 (2012) 331–349.
[7] R.P. Lefojane, B.T. Sone, N. Matinise, K. Saleh, P. Direko, P. Mfengwana, S. Mashele, M. Maaza, M.P. Sekhoacha, CdO/$CdCO_3$ nanocomposite physical properties and cytotoxicity against selected breast cancer cell lines, Sci. Rep., 11 (2021) 30, doi: 10.1038/s41598-020-78720-5.
[8] F.M. Castañeda de la Hoya, R. Castanedo-Pérez, J. Márquez-Marín, F.A. Hernández-García, G. Torres-Delgado, Study of the water content on the CdO + $CdTiO_3$ crystalline grains distribution in thin films obtained by sol–gel and their effect on the morphological, optical, and photocatalytic properties, Colloids Surf., A, 662 (2023) 131033, doi: 10.1016/j.colsurfa.2023.131033.
[9] O. Ali Al Hattali, F. Al Marzouqi, S. Al Mamari, A.T. Kuvarega, R. Selvaraj, CdO nanoplates for photocatalytic degradation of Levofloxacin and Nizatidine under natural solar light irradiation, Inorg. Chem. Commun., 146 (2022) 110071, doi: 10.1016/j.inoche.2022.110071.
[10] Tripta, P.S. Rana, Suman, Tuning the morphological, optical, electrical, and structural properties of $NiFe_2O_4$@CdO nanocomposites and their photocatalytic application, Ceram. Int., 49 (2023) 18735–18744.
[11] A.A. Dakhel, Transparent conducting properties of samarium-doped CdO, J. Alloys Compd., 475 (2009) 51–54.

[12] A.A. Dakhel, Electrical and optical properties of iron-doped CdO, Thin Solid Films, 518 (2010) 1712–1715.
[13] J. Li, Y. Ni, J. Liu, J. Hong, Preparation, conversion, and comparison of the photocatalytic property of $Cd(OH)_2$, CdO, CdS and CdSe, J. Phys. Chem. Solids, 70 (2009) 1285–1289.
[14] A. Tadjarodi, M. Imani, H. Kerdari, Experimental design to optimize the synthesis of CdO cauliflower-like nanostructure and high performance in photodegradation of toxic azo dyes, Mater. Res. Bull., 48 (2013) 935–942.
[15] S. Sivakumar, A. Venkatesan, P. Soundhirarajan, C.P. Khatiwada, Synthesis, characterizations and anti-bacterial activities of pure and Ag doped CdO nanoparticles by chemical precipitation method, Spectrochim. Acta, Part A, 136 (2015) 1751–1759.
[16] V.K. Gupta, A. Fakhri, S. Tahami, S. Agarwal, Zn doped CdO nanoparticles: structural, morphological, optical, photo-catalytic and anti-bacterial properties, J. Colloid Interface Sci., 504 (2017) 164–170.
[17] R. Saravanan, H. Shankar, T. Prakash, V. Narayanan, A. Stephen, ZnO/CdO composite nanorods for photocatalytic degradation of methylene blue under visible light, Mater. Chem. Phys., 125 (2011) 277–280.
[18] S. Kumar, A.K. Ojha, B. Walkenfort, Cadmium oxide nanoparticles grown in situ on reduced graphene oxide for enhanced photocatalytic degradation of methylene blue dye under ultraviolet irradiation, J. Photochem. Photobiol., B, 159 (2016) 111–119.
[19] P. Dhatshanamurthi, B. Subash, M. Shanthi, Investigation on UV-A light photocatalytic degradation of an azo dye in the presence of CdO/TiO_2 coupled semiconductor, Mater. Sci. Semicond. Process., 35 (2015) 22–29.
[20] T. Linda, S. Muthupoongodi, X.S. Shajan, S. Balakumar, Fabrication and characterization of chitosan templated CdO/NiO nano composite for dye degradation, Optik, 127 (2016) 8287–8293.
[21] C. Venkata Reddy, N. Bandaru, J. Shim, S.V.P. Vattikuti, Synthesis of CdO/ZnS heterojunction for photodegradation of organic dye molecules, Appl. Phys. A, 123 (2017) 396, doi: 10.1007/s00339-017-1013-3.
[22] D.J. Jeejamol, K.S. Jai Aultrin, M. Dev Anand, Exploration of CdO properties favoring superior photocatalytic degradation of methylene blue dye by Al^{3+} doping, Opt. Quantum Electron., 54 (2022) 291, doi: 10.1007/s11082-022-03694-9.
[23] M. Mansour, I. Benyamina, B. Benalioua, A. Bentouami, B. Boury, H. Hentit, P.-E. Lippens, Combined effect between PVP and glass wool for improvement of the photocatalytic activity under visible light of bismuth(III) oxyhalide and access to α-Bi_2O_3-BiOI-BiOBr, Appl. Surf. Sci., 534 (2020) 147577, doi: 10.1016/j.apsusc.2020.147577.
[24] C. Li, Y. Ma, S. Zheng, C. Hu, F. Qin, L. Wei, C. Zhang, S. Duo, Q. Hu, One-pot synthesis of Bi_2O_3/Bi_2O_4 p-n heterojunction for highly efficient photocatalytic removal of organic pollutants under visible light irradiation, J. Phys. Chem. Solids, 140 (2020) 109376, doi: 10.1016/j.jpcs.2020.109376.
[25] A. Aranda-Aguirre, J.M. de Oca, A. Corzo, S. Garcia-Segura, H. Alarcon, Mixed metal oxide Bi_2O_3/Bi_2WO_6 thin films for the photoelectrocatalytic degradation of histamine, J. Electroanal. Chem., 919 (2022) 116528, doi: 10.1016/j.jelechem.2022.116528.
[26] Y. Zhang, M. Zhu, S. Zhang, Y. Cai, Z. Lv, M. Fang, X. Tan, X. Wang, Highly efficient removal of U(VI) by the photoreduction of $SnO_2/CdCO_3/CdS$ nanocomposite under visible light irradiation, Appl. Catal., B, 279 (2020) 119390, doi: 10.1016/j.apcatb.2020.119390.
[27] S.G. Ruvalcaba-Manzo, S.J. Castillo, R. Ochoa-Landín, M. Flores-Acosta, R. Ramírez-Bon, Optical, structural, and morphological characterization of cadmium carbonate thin films by CBD two formulations, Opt. Mater., 109 (2020) 110295, doi: 10.1016/j.optmat.2020.110295.
[28] I. Benyamina, K. Manseri, M. Mansour, B. Benalioua, A. Bentouami, B. Boury, New Bi_2O_3-ZnO composite deposited on glass wool. Effect of the synthesis method on photocatalytic efficiency under visible light, Appl. Surf. Sci., 483 (2019) 859–869.
[29] N. Premalatha, L. Rose Miranda, Surfactant modified ZnO–Bi_2O_3 nanocomposite for degradation of lambda-cyhalothrin pesticide in visible light: a study of reaction kinetics and intermediates, J. Environ. Manage., 246 (2019) 259–266.
[30] S. Ramachandran, A. Sivasamy, Effective charge separation in binary ZnO-Bi_2O_3 photocatalytic material for the treatment of simulated wastewater, Mater. Today Proc., 17 (2019) 101–110.
[31] B.T. Huy, D.S. Paeng, C. Thi Bich Thao, N.T. Kim Phuong, Y.-I. Lee, ZnO-Bi_2O_3/graphitic carbon nitride photocatalytic system with H_2O_2-assisted enhanced degradation of Indigo carmine under visible light, Arabian J. Chem., 13 (2020) 3790–3800.
[32] N. Lakshmana Reddy, G. Krishna Reddy, K. Mahaboob Basha, P. Krishna Mounika, M.V. Shankar, Highly efficient hydrogen production using Bi_2O_3/TiO_2 nanostructured photocatalysts under led light irradiation, Mater. Today Proc., 3 (2016) 1351–1358.
[33] Q. Huang, J. Ye, H. Si, B. Yang, T. Tao, Y. Zhao, M. Chen, H. Yang, Differences of characteristics and performance with Bi^{3+} and Bi_2O_3 doping over TiO_2 for photocatalytic oxidation under visible light, Catal. Lett., 150 (2020) 1098–1110.
[34] H. Rongan, L. Haijuan, L. Huimin, X. Difa, Z. Liuyang, S-scheme photocatalyst Bi_2O_3/TiO_2 nanofiber with improved photocatalytic performance, J. Mater. Sci. Technol., 52 (2020) 145–151.
[35] D. Wu, M. Long, Realizing visible-light-induced self-cleaning property of cotton through coating N-TiO_2 film and loading AgI particles, ACS Appl. Mater. Interfaces, 3 (2011) 4770–4774.
[36] G. Xiao, X. Huang, X. Liao, B. Shi, One-pot facile synthesis of cerium-doped TiO_2 mesoporous nanofibers using collagen fiber as the biotemplate and its application in visible light photocatalysis, J. Phys. Chem. C, 117 (2013) 9739–9746.
[37] H.F. Moafi, A.F. Shojaie, M.A. Zanjanchi, Titania and titania nanocomposites on cellulosic fibers: synthesis, characterization and comparative study of photocatalytic activity, Chem. Eng. J., 166 (2011) 413–419.
[38] D.-H. Yu, X. Yu, C. Wang, X.-C. Liu, Y. Xing, Synthesis of natural cellulose-templated TiO_2/Ag nanosponge composites and photocatalytic properties, ACS Appl. Mater. Interfaces, 4 (2012) 2781–2787.
[39] T.-D. Pham, B.-K. Lee, Feasibility of silver doped TiO_2/glass fiber photocatalyst under visible irradiation as an indoor air germicide, Int. J. Environ. Res. Public Health, 11 (2014) 3271–3288.
[40] T.-D. Pham, B.-K. Lee, Cu doped TiO_2/GF for photocatalytic disinfection of *Escherichia coli* in bioaerosols under visible light irradiation: application and mechanism, Appl. Surf. Sci., 296 (2014) 15–23.
[41] P. Kongsong, L. Sikong, S. Niyomwas, V. Rachpech, Photocatalytic antibacterial performance of glass fibers thin film coated with N-doped SnO_2/TiO_2, Sci. World J., 2014 (2014) 869706, doi: 10.1155/2014/869706.
[42] R.J. Tayade, R.G. Kulkarni, R.V. Jasra, Enhanced photocatalytic activity of TiO_2-coated NaY and HY zeolites for the degradation of methylene blue in water, Ind. Eng. Chem. Res., 46 (2007) 369–376.
[43] H. Zhang, X. Lv, Y. Li, Y. Wang, J. Li, P25-graphene composite as a high performance photocatalyst, ACS Nano, 4 (2010) 380–386.
[44] S.D. Perera, R.G. Mariano, K. Vu, N. Nour, O. Seitz, Y. Chabal, K.J. Balkus, Hydrothermal synthesis of graphene-TiO_2 nanotube composites with enhanced photocatalytic activity, ACS Catal., 2 (2012) 949–956.
[45] W. Qian, P.A. Greaney, S. Fowler, S.-K. Chiu, A.M. Goforth, J. Jiao, Low-temperature nitrogen doping in ammonia solution for production of N-doped TiO_2-hybridized graphene as a highly efficient photocatalyst for water treatment, ACS Sustainable Chem. Eng., 2 (2014) 1802–1810.
[46] C. Chen, W. Cai, M. Long, B. Zhou, Y. Wu, D. Wu, Y. Feng, Synthesis of visible-light responsive graphene oxide/TiO_2 composites with p/n heterojunction, ACS Nano, 4 (2010) 6425–6432.

[47] M.S.A. Sher Shah, A.R. Park, K. Zhang, J.H. Park, P.J. Yoo, Green synthesis of biphasic TiO_2–reduced graphene oxide nanocomposites with highly enhanced photocatalytic activity, ACS Appl. Mater. Interfaces, 4 (2012) 3893–3901.
[48] B. Benalioua, I. Benyamina, M. Mansour, K. Mensri, A. Bentouami, B. Boury, Synthesis of a new multi-heterojunction photocatalyst BiOI/Bi_2O_3/MgO, and its photocatalytic efficiency in the degradation of Rhodamine B under visible light, Desal. Water Treat., 281 (2023) 265–275.
[49] F.-t. Li, X.-j. Wang, Y. Zhao, J.-x. Liu, Y.-j. Hao, R.-h. Liu, D.-s. Zhao, Ionic-liquid-assisted synthesis of high-visible-light-activated N–B–F-tri-doped mesoporous TiO_2 via a microwave route, Appl. Catal., B, 144 (2014) 442–453.
[50] G.-D. Lim, J.-H. Yoo, M. Ji, Y.-I. Lee, Visible light driven photocatalytic degradation enhanced by α/β phase heterojunctions on electrospun Bi_2O_3 nanofibers, J. Alloys Compd., 806 (2019) 1060–1067.
[51] Y. Jia, X.-Y. Yu, T. Luo, J.-H. Liu, X.-J. Huang, Shape-controlled synthesis of $CdCO_3$ microcrystals and corresponding nanoporous CdO architectures, RSC Adv., 2 (2012) 10251–10254.
[52] S. Landi, I.R. Segundo, E. Freitas, M. Vasilevskiy, J. Carneiro, C.J. Tavares, Use and misuse of the Kubelka–Munk function to obtain the band gap energy from diffuse reflectance measurements, Solid State Commun., 341 (2022) 114573, doi: 10.1016/j.ssc.2021.114573.
[53] H. Jamil, I.M. Dildar, U. Ilyas, J.Z. Hashmi, S. Shaukat, M.N. Sarwar, M. Khaleeq-ur-Rahman, Microstructural and optical study of polycrystalline manganese oxide films using Kubelka–Munk function, Thin Solid Films, 732 (2021) 138796, doi: 10.1016/j.tsf.2021.138796.
[54] A. Escobedo-Morales, I.I. Ruiz-López, M.d. Ruiz-Peralta, L. Tepech-Carrillo, M. Sánchez-Cantú, J.E. Moreno-Orea, Automated method for the determination of the band gap energy of pure and mixed powder samples using diffuse reflectance spectroscopy, Heliyon, 5 (2019) e01505, doi: 10.1016/j.heliyon.2019.e01505.
[55] N. Sangiorgi, L. Aversa, R. Tatti, R. Verucchi, A. Sanson, Spectrophotometric method for optical band gap and electronic transitions determination of semiconductor materials, Opt. Mater., 64 (2017) 18–25.
[56] C. Xu, X. Wang, J. Zhu, Graphene–metal particle nanocomposites, J. Phys. Chem. C, 112 (2008) 19841–19845.
[57] T. Szabó, O. Berkesi, P. Forgó, K. Josepovits, Y. Sanakis, D. Petridis, I. Dékány, Evolution of surface functional groups in a series of progressively oxidized graphite oxides, Chem. Mater., 18 (2006) 2740–2749.
[58] J.I. Paredes, S. Villar-Rodil, P. Solís-Fernández, A. Martínez-Alonso, J.M.D. Tascón, Atomic force and scanning tunneling microscopy imaging of graphene nanosheets derived from graphite oxide, Langmuir, 25 (2009) 5957–5968.
[59] C. Shan, H. Yang, J. Song, D. Han, A. Ivaska, L. Niu, Direct electrochemistry of glucose oxidase and biosensing for glucose based on graphene, Anal. Chem., 81 (2009) 2378–2382.
[60] X. Liu, H. Deng, W. Yao, Q. Jiang, J. Shen, Preparation and photocatalytic activity of Y-doped Bi_2O_3, J. Alloys Compd., 651 (2015) 135–142.
[61] S. Zhu, L. Lu, Z. Zhao, T. Wang, X. Liu, H. Zhang, F. Dong, Y. Zhang, Mesoporous Ni-doped δ-Bi_2O_3 microspheres for enhanced solar-driven photocatalysis: a combined experimental and theoretical investigation, J. Phys. Chem. C, 121 (2017) 9394–9401.
[62] S.D. Khairnar, A.N. Kulkarni, S.G. Shinde, S.D. Marathe, Y.V. Marathe, S.D. Dhole, V.S. Shrivastava, Synthesis and characterization of 2-D La-doped Bi_2O_3 for photocatalytic degradation of organic dye and pesticide, J. Photochem. Photobiol., 6 (2021) 100030, doi: 10.1016/j.jpap.2021.100030.
[63] T. Munawar, M.N. ur Rehman, M.S. Nadeem, F. Mukhtar, S. Manzoor, M.N. Ashiq, F. Iqbal, Facile synthesis of Cr-Co co-doped CdO nanowires for photocatalytic, antimicrobial, and supercapacitor applications, J. Alloys Compd., 885 (2021) 160885, doi: 10.1016/j.jallcom.2021.160885.
[64] R.K. Mandal, P. Saha, T.P. Majumder, Structural, optical characterization of the synthesized Fe doped CdO nano particles, its application as a promising photocatalyst for degradation of the hazardous methyl violet dye, Optik, 246 (2021) 167795, doi: 10.1016/j.ijleo.2021.167795.